SUPPLEMENTAL MATERIAL

Magnetic-field amplification in supersonic laser-plasma turbulence

Bott et al.

TECHNICAL SPECIFICATION OF EXPERIMENTAL PLATFORM

The targets that are employed in our experiment (cf. Figure 1 of the main text) have the following specifications. The aluminum foils that are irradiated by the LMJ drive beams have a 3 mm diameter and 25 μm thickness. An annular CH washer (230 μm thick, 3 mm diameter, 400 μm hole) is placed over the foil to aid jet collimation. The grids (located 2 mm away from each foil, on the opposite side to the LMJ beams) are made of polyamide, have a thickness of 250 μm, and square holes (side length 300 μm) separated by 100 μm rods. The proton source is a 50 μm gold foil, and is protected from pre-plasma and return currents by an aluminium polycarbonate shield. It is located 3 cm from the turbulent plasma's centre. The RCF stack used to detect the protons after they pass through the plasma is placed 10 cm away on the opposite side, leading to a $\times 4.3$ magnification. All length scales that are shown in the main text have this magnification factor removed, i.e., on the plasma's scale.

As for the laser beam specification, the LMJ beams have a wavelength of 351 nm, a pulse length of 5 ns, and deliver 20 kJ of energy per (aluminum) foil. The PETAL short-pulse beam that we employ for the proton-imaging diagnostic, CRACC, has a wavelength of 1053 nm, a pulse length of 650 fs, and delivers 350 J of energy to the gold-foil target. We note that in the shot during which the 15.7 ns proton image was obtained, a 30% drop in the laser energy (14 kJ per foil vs. 20 kJ per foil) delivered to both foils by LMJ was recorded, due to a technical failure; an identical drop on one foil was recorded in the shot during which the 22.7 ns proton image was obtained. However, we do not believe that our results are significantly affected by this (see next section).

EFFECT OF SUPPRESSED LASER PERFORMANCE ON RESULTS

Our belief that the change in the delivered LMJ drive-beam energy (see previous section) does not significantly affect our results is based on the following claim: that, for our experimental parameters, the initial velocity of the rear-side-blow-off plasma jet is only weakly sensitive to the drive beam energy. This claim can be justified as follows. Given a laser focal-spot diameter of 300 μm, a pulse length of 5 ns, and a total beam energy of 20 kJ per foil, the laser intensity I_L is given by $I_L \approx 5.6 \times 10^{15}\,\mathrm{W\,cm^{-2}}$. For a laser wavelength $\lambda_L = 351$ nm and laser intensities $I_L \sim 10^{13}$–$10^{15}\,\mathrm{W\,cm^{-2}}$, a simple physical argument [1] suggests that the ablation pressure P_{ab} approximately scales with I_L via $P_{\mathrm{ab}} \propto I_L^{2/3}$ – a scaling which has been (approximately) verified experimentally (see, for example, [2]). In turn, simple scaling arguments show that the characteristic velocity $u_{\mathrm{jet}}(s)$ of the rear-side-blow-off plasma jet at displacement s from its initial position is related to P_{ab} by $u_{\mathrm{jet}}(s) \sim \sqrt{P_{\mathrm{ab}} s/\delta_{\mathrm{t}}\rho_{\mathrm{t}}}$, where δ_{t} is the thickness of the target foil onto which the laser is incident, and ρ_{t} is the foil density. This implies that $u_{\mathrm{jet}}(s) \propto I_L^{1/3}$. In short, a $\sim 30\%$ reduction in the laser intensity only results in a modest ($\sim 10\%$) reduction in the initial jet velocity. In fact, for the characteristic intensities employed in this experiment – for our laser parameters, $[I_L(\mathrm{W\,cm^{-2}})/10^{15}\,\mathrm{W\,cm^{-2}}][\lambda_L(\mu\mathrm{m})/1\,\mu\mathrm{m}]^2 \approx 0.7$ – the dependence of the ablation pressure on the laser intensity is likely even weaker, on account of various physical phenomena (nonlinear inverse Bremsstrahlung and resonant plasma instabilities) that reduce absorption efficiency as the intensity is increased further [3]. In consequence, the error induced in our results by the drop in delivered laser energy is less than 10%; this is smaller than the reported error of our measurements.

There is also qualitative experimental evidence that the suppressed laser performance does not affect our results: specifically, the central location of proton-flux inhomogeneities in the ∼22.7 ns proton image (see Figure 4). As stated earlier, the drive on one of the foils was 30% lower than on the other foil in the experimental shot during which this data was collected; if this drop in energy affected the initial velocity of one of the plasma jets, it would be anticipated that the collision of the two jets would happen off-center. However, the mean positions of the proton-flux inhomogeneities in the 19.7-ns and 22.7-ns proton images were, in fact, very similar.

ADDITIONAL INFORMATION ON PROTON-IMAGE ANALYSIS

Extracting proton flux measurements from RCF film pack

We convert the raw RCF images obtained in our experiment to (normalised) proton flux images using the following procedure. The RCF (HD-V2) films are electronically scanned, and then converted into 300-dots-per-inch RGB TIFF files. The red colour channel of these files is transformed to an optical density image, and then to a deposited energy ($\mathrm{MeV/mm^2}$) image using an appropriate calibration for our chosen RCF film type. A GEANT-4 simulation [4] was then carried out, in order to determine the relationship between the energy deposited in each piece of film by a

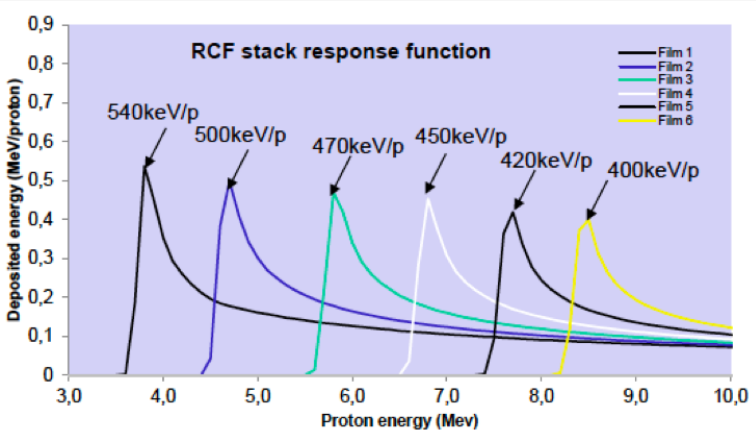

Supplementary Figure 1: *RCF stack response functions.* Relationship between the energy deposited in a given film layer by an imaging proton, and that proton's energy.

given proton, and that proton's energy. Curves showing this relationship ('the RCF response function') for the six distinct pieces of RCF film used in our experiment are shown in Supplementary Figure 1. Finally, an estimate of the proton flux is made by assuming that the majority of the energy deposited in each film comes from the protons that deposit the maximum energy associated with that particular piece of film. Table I shows this energy for each film layer. Such an estimate is justified (even though protons with a range of speeds deposit their energy in a given

HD-V2 film layer	$\epsilon_{p,\mathrm{max}}$ (MeV)	$\epsilon_{p,\mathrm{dep}}$ (MeV/proton)
1	3.8	0.54
2	4.7	0.50
3	5.8	0.47
4	6.8	0.45
5	7.7	0.42
6	8.5	0.40

Supplementary Table I: Characterisation of our RCF film pack, using GEANT-4 simulations. Here, $\epsilon_{p,\mathrm{max}}$ is the proton energy at which energy deposition in a given film layer is maximised, and $\epsilon_{p,\mathrm{dep}}$ is the deposited energy for such protons.

layer of the RCF stack) by the following argument. In any given film layer, the energy $\epsilon_{p,\mathrm{dep}}$ deposited by protons with incident energy ϵ_p drops to $< 50\%$ of the peak deposited-energy value given in the final column of Table I for $|\epsilon_p - \epsilon_{p,\mathrm{max}}| \gtrsim 0.25\,\mathrm{MeV}$. As a result, the full-half-width-maximum (FHWM) $\Delta\epsilon_{p,\mathrm{max}}$ is much smaller than $\epsilon_{p,\mathrm{max}}$. Protons with incident energy $\epsilon_p < \epsilon_{p,\mathrm{max}} - 0.5\,\mathrm{MeV}$ do not deposit any energy at all, because they do not reach the film layer. On the other hand, protons with incident energy $\epsilon_p \gtrsim \epsilon_{p,\mathrm{max}} + 0.25\,\mathrm{MeV}$ could, in principle, deposit 20–50% of the maximum deposited energy. However, in the experiment, the energy distribution of the proton-imaging beam is exponential, with a characteristic temperature of $\sim$3 MeV; as a result, the contribution of protons with higher energies is suppressed further, due to their lower number. The proton images resulting from this (with flux values normalised to the mean value in the region between the grids) for each of our experimental shots are shown in Figures 2, 3 and 4.

Recovering path-integrated magnetic fields from proton flux measurements

In this section, we provide additional details about our analysis of the proton images. The reconstruction of the path-integrated magnetic field from a given proton image is carried out using the algorithm described in [5] (see also the Supplementary Information of [6]); however, here we clarify a few details of the analysis specific to this experiment.

First, we note that, similarly to related experiments that employed a proton-imaging diagnostic to measure turbulent amplification of magnetic fields [6], both collisionless beam instabilities and deflections due to electric fields in this experiment have a negligible effect on the proton-imaging beam. Electrostatic beam instabilities cannot act effectively

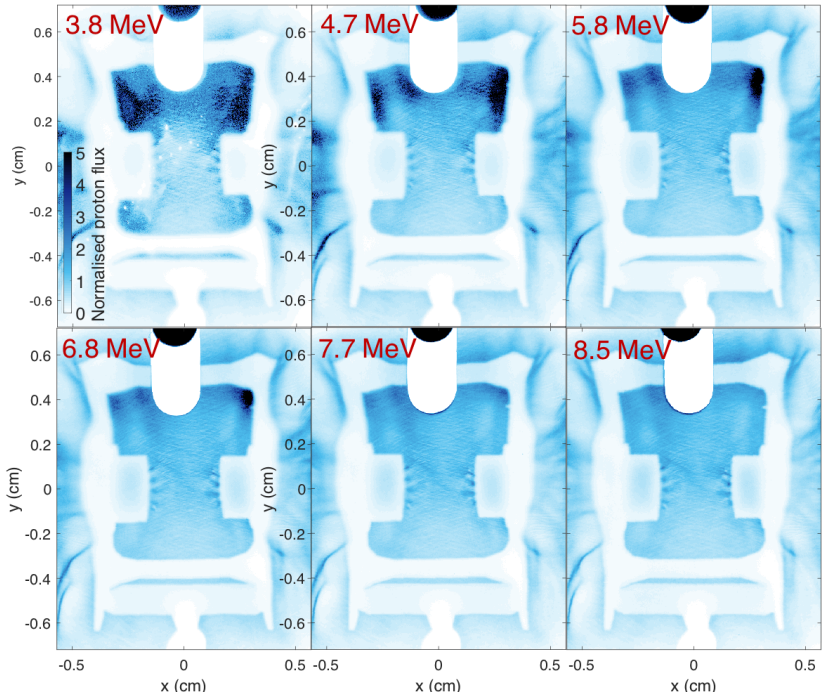

Supplementary Figure 2: *Normalised proton flux images for the first experimental shot.* In this experimental shot, the fastest species of imaging proton traverses the plasma ~ 15.7 ns after the LMJ drive beams are initiated. The energy associated with maximal deposited energy per proton is given in the top left-hand corner of each panel.

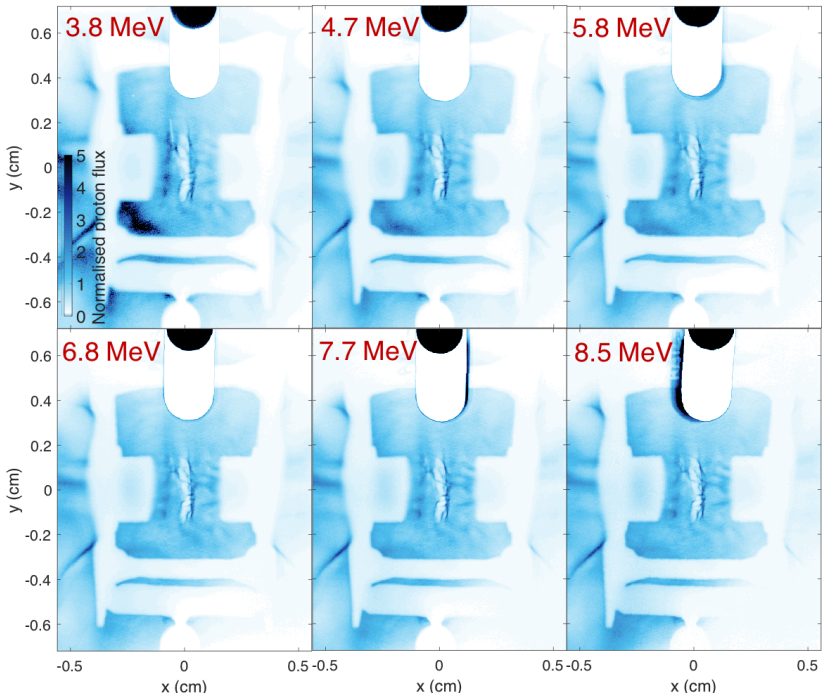

Supplementary Figure 3: *Normalised proton flux images for the second experimental shot.* The same as Supplementary Figure 2, except with the fastest species of imaging proton traversing the plasma ~ 19.7 ns after the LMJ drive beams are initiated.

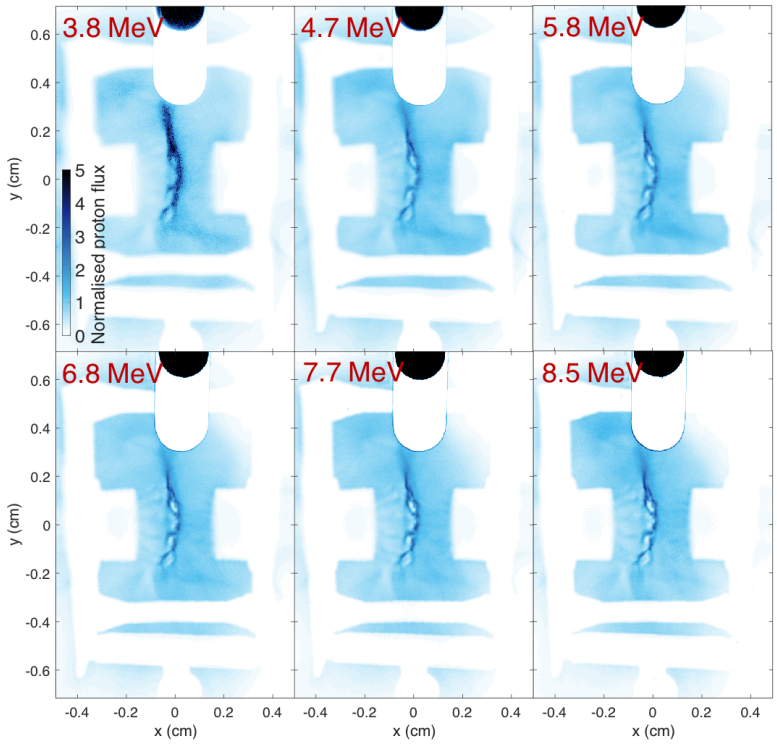

Supplementary Figure 4: *Normalised proton flux images for the third experimental shot.* The same as Supplementary Figure 2, except with the fastest species of imaging proton traversing the plasma ~ 22.7 ns after the LMJ drive beams are initiated.

because the number density of the proton beam is many orders of magnitude smaller than that of the turbulent plasma's thermal electron population (see Appendix D of [8]); deflections due to stochastic electric fields whose characteristic scale is the grid periodicity $L = 0.04$ cm are much weaker than those due to magnetic fields, because the characteristic speed of the imaging protons is much faster than that of stochastic motions at scale L in the plasma (see Appendix B of [5]). It is therefore appropriate to use the algorithm described in [5] to reconstruct path-integrated magnetic fields from our proton images (albeit given certain caveats, which are discussed in the next paragraph).

Next, we explain why we chose to present only the analysis carried out on the proton images arising from the sixth RCF film layer (8.5 MeV protons) for all of our experimental shots, and for the second RCF film layer (4.7 MeV) for the experimental shot characterizing our experiment prior to collision. As stated in the main text, quantitative analysis of a given proton image using the approach described in [5] is only possible if the proton beam does not self-intersect (due to deflections acquired in the plasma) prior to reaching the detector. Such self-intersection can be identified by certain features present in proton images (see [5] for an extended discussion). One such feature is the presence of localised proton-flux 'structures' with two key properties: first, typical values much higher than the mean proton flux in an image; second, the broadening of those structures in lower-energy proton images of the same fields. Such a feature can indeed be identified in our proton images for the (two) experimental shots subsequent to the collision of the jets in our experiment. This suggests that so-called 'caustics' are present in all but the highest-energy proton image, and thus the quantitative analysis technique proposed in [5] cannot be carried out reliably on the proton images derived from the first five film layers. By contrast, the variations in proton flux for the experimental shot prior to the jet collision do not have this feature, and so all film layers can, in principle, be analyzed. However, the first layer (see Supplementary Figure 2, top left) has other features suggestive of the film layer being damaged: so a quantitative analysis of such an image would likely lead to erroneous results. As the protons detected in second film layer arrive with the greatest time difference from the sixth layer, we chose to focus our analysis on these two layers for this shot.

Thirdly, we discuss our approach to characterizing the initial proton beam's flux distribution – necessary input into any magnetic-field-reconstruction algorithm. It is known that proton beams arising from high-intensity laser sources can have significant spatial variation prior to any interaction with electromagnetic fields [9]. However, such variation

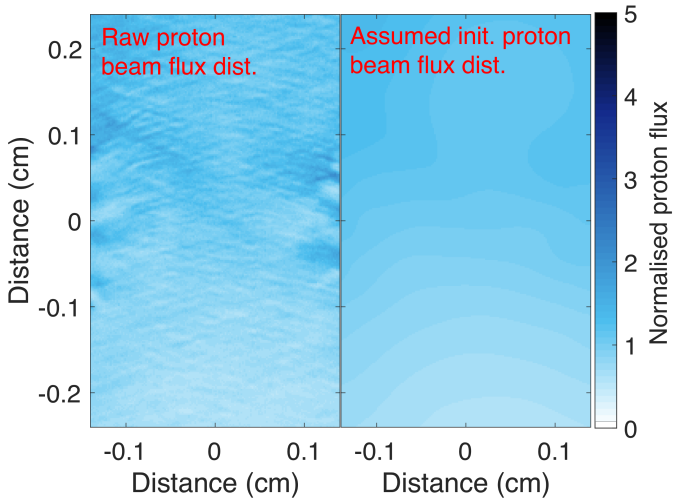

Supplementary Figure 5: *Assumed initial proton-beam flux distribution.* Left: rectangular sample from the 8.5 MeV proton image at ∼15.7 ns. The sample is the same as the region depicted in the bottom left of Figure 1 of the main text. Right: assumed initial 8.5 MeV proton-beam flux distribution employed for recovering path-integrated magnetic field (which is calculated using the approach described in the accompanying text).

is typically on much larger scales than strong variations in proton flux – so we assume that all variations on scales larger than the known physical scales of interest (i.e., the interaction region's size, $\ell_{n\perp} \approx 0.25\,\mathrm{cm}$) are variations in the initial proton flux. We determine these initial variations in a two-step procedure: we first calculate a (two dimensional) linear best fit; we then apply a low-pass filter to the difference between the flux distribution and the linear fit (with characteristic filtering scale $\ell = 1.5\ell_{n\perp}$). The result is illustrated in Supplementary Figure 5. The path-integrated field is then reconstructed using the usual technique described in [5]; in order to be consistent with our previous assumptions, we apply a Gaussian high-pass filter to the path-integrated fields with the same parameters at the low-pass filter applied to the original proton image.

Fourth, we briefly discuss the implications of assuming that the measured proton images are created using a monoenergetic beam (with energy $\epsilon_{p,\mathrm{max}}$) when we apply the field-reconstruction algorithm, despite our statement in the previous section that protons with a distribution of energies (the characteristic dispersion of that energy around the mean, $\Delta\epsilon_{p,\mathrm{max}}$, being $\Delta\epsilon_{p,\mathrm{max}} \approx 0.5$–$1$ MeV) contribute significantly to the deposited energy in each film layer of the RCF film stack. The uncertainty in the imaging protons' energy leads to an uncertainty in the deflection angles of the protons composing a particular proton image; for deflections induced by magnetic fields (where the deflection angle, α_p, satisfies $\alpha_p \propto \epsilon_p^{-1/2}$), this uncertainty is of order $\sim\Delta\epsilon_{p,\mathrm{max}}/2\epsilon_{p,\mathrm{max}}$. Therefore, the path-integrated magnetic field measurements derived from the second film layer have an ∼15% intrinsic uncertainty due to this effect, while those from the sixth film layer have an ∼5% uncertainty. The latter error is a small fraction of the error (∼20–30%) of magnetic-field measurements of the interaction-region plasma (which are all derived from the sixth film layer) arising from other sources of uncertainty in the experiment, suggesting that the monoenergetic assumption is a reasonable one for us to make.

The 'total' path-integrated magnetic fields recovered from the proton images obtained after collision of the plasma jets are shown in Supplementary Figure 6. In the main text, we report 'large-scale' – that is, at the scale of the interaction region – and 'small-scale' – at the characteristic scale of the turbulence, and at smaller scales – path-integrated fields. In order to recover the large-scale (small-scale) path-integrated magnetic fields from the total path-integrated fields, we apply an additional low-pass (high-pass) filter. The choice of filter is complicated by the fact that the morphology of the interaction region is anisotropic: its parallel size $\ell_{n\parallel} \approx 400\,\mu\mathrm{m}$ is much smaller than its perpendicular size ($\ell_{n\perp} \approx 2.5\,\mathrm{mm}$). We therefore apply an anisotropic Gaussian low-pass filter (scale parameters $\ell_\parallel$ and $\ell_\perp$ at particular times given in the caption of Supplementary Figure 6) to obtain the large-scale field, and an anisotropic Gaussian high-pass filter (same parameters) to extract the small-scale field. We note that since the parallel size of the interaction region is rather similar to the scale associated with the peak wavenumber of the magnetic-energy spectra, it is possible that some magnetic structures associated with the supersonic turbulence whose

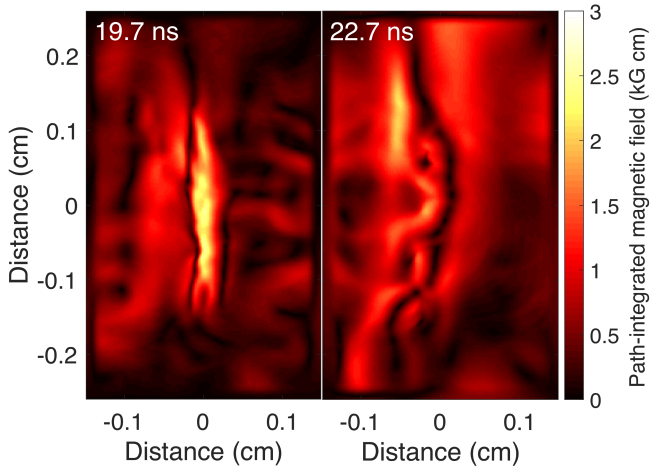

Supplementary Figure 6: *Magnitude of total path-integrated magnetic fields recovered from post-collision proton images.* Left: total path-integrated magnetic field recovered from 8.5 MeV proton image taken at ∼19.7 ns after the initiation of the LMJ drive beams. The scale parameters $\ell_\parallel$ and $\ell_\perp$ of the anisotropic Gaussian low- and high-pass filters used to recover 'large-scale' and 'small-scale' components of the path-integrated field (shown in Figure 4 of the main text) are given by $\ell_\parallel = 0.018\,\mathrm{cm}$, $\ell_\perp = 0.15\,\mathrm{cm}$. Right: total path-integrated magnetic field recovered from 8.5 MeV proton image taken at ∼22.7 ns. The anisotropic Gaussian filter parameters used in this case are $\ell_\parallel = 0.088\,\mathrm{cm}$, $\ell_\perp = 0.2\,\mathrm{cm}$.

associated wavevectors are oriented in the parallel direction will be suppressed by the high-pass filter. However, for an isotropic stochastic magnetic field, the resulting underestimate of the RMS value of the field will only be a small correction (of order $\sim \ell_\parallel/\ell_\perp \lesssim 15\%$).

To illustrate how the large-scale and small-scale path-integrated magnetic fields relate back to the proton images from which they were extracted, we show the proton images resulting from the large- and small- scale fields individually in Figure 7. For comparison, we also show the original proton images, and the predicted images associated with the total path-integrated magnetic field. It is qualitatively clear that the stochastic, smale-scale flux structures in the original proton images are indeed reproduced by imaging the small-scale path integrated field; however, the presence of the large-scale field distorts both their shape and position.

Electron number density measurements using collisional scattering of imaging protons

Here, we elaborate on how we obtained the measurements of electron number density of the interaction-region plasma using collisional scattering of the proton imaging beam; we also provide a bound on the electron number density of the initial supersonic plasma jets on account of the absence of such scattering.

First, we outline the relationship between the effective proton-image resolution and the plasma's electron number-density. A beam of protons (initial speed V_0) travelling through a plasma with electron number density n_e diffuses in the direction(s) transverse to its initial motion due to small-angle Coulomb collisions. The characteristic spread in velocities $\Delta v_\perp$ in the proton beam associated with these collisions evolves according to

$$\frac{\mathrm{d}\Delta v_\perp^2}{\mathrm{d}t} = \left(\nu_\perp^{p|\mathrm{Al}} + \nu_\perp^{p|e}\right) v^2\,, \tag{1}$$

where v is the speed of the proton beam after time t of its interaction with the plasma, $\nu_\perp^{p|\mathrm{Al}}$ is the characteristic perpendicular diffusion rate due to Coulomb collisions with aluminium ions, and $\nu_\perp^{p|e}$ is the characteristic perpendicular diffusion rate due to Coulomb collisions with electrons [10]. For the protons used in our experiment, whose velocity is $V_0 \gtrsim 3\times10^9\,\mathrm{cm/s}$, the beam protons' velocities greatly exceed both the plasma's thermal ion and electron velocities (assuming a jet-plasma temperature $T \approx 100$ eV); as a consequence, $\nu_\perp^{p|\mathrm{Al}}$ and $\nu_\perp^{p|e}$ are given by the fast test particle

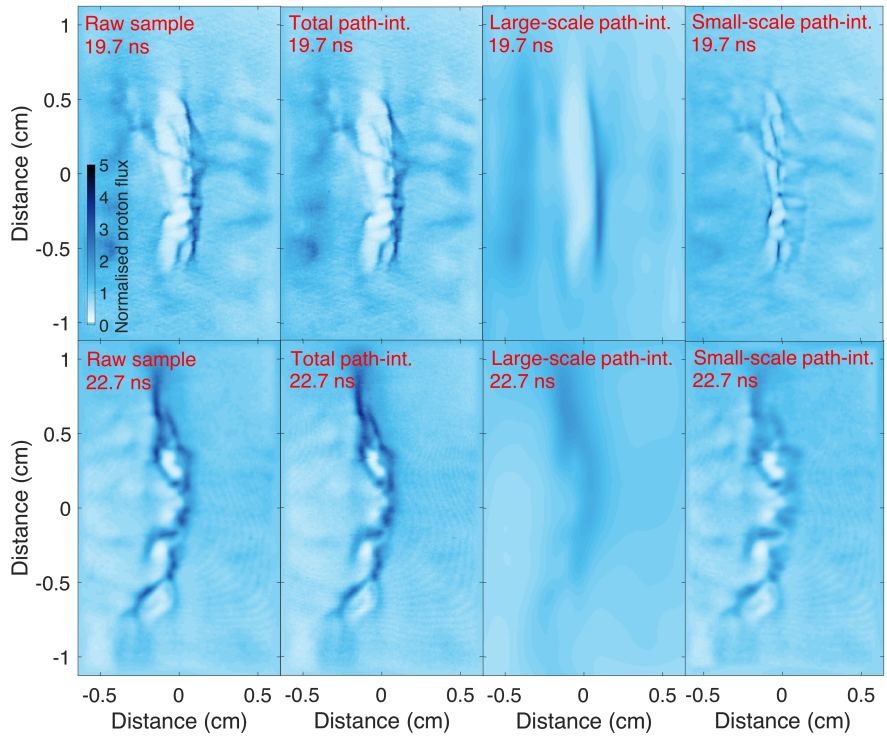

Supplementary Figure 7: *Predicted 8.5 MeV proton images resulting from recovered path-integrated magnetic fields.* Top far-left: sample from 19.7 ns, 8.5 MeV proton image, used for recovering the path-integrated magnetic field. Top mid-left: proton-flux distribution arising from the total path-integrated magnetic field at 19.7 ns (which is presented in Supplementary Figure 6, left). Top mid-right: proton-flux distribution arising from the large-scale path-integrated field at 19.7 ns (which is presented in Figure 4 of the main text, top left). Top far-right: proton flux distribution arising from the small-scale path-integrated field at 19.7 ns (presented in Figure 4 of the main text, top mid-left). Bottom far-left: sample from 22.7 ns, 8.5 MeV proton image. Bottom mid-left: proton-flux distribution arising from the total path-integrated field at 22.7 ns (presented in Supplementary Figure 6, right). Bottom mid-right: proton-flux distribution arising from the large-scale path-integrated field at 22.7 ns (presented in Figure 4 of the main text, bottom left). Bottom far-right: proton-flux distribution arising from the small-scale path-integrated field at 22.7 ns (presented in Figure 4 of the main text, bottom mid-left).

rates:

$$\nu_\perp^{p|\mathrm{Al}} \approx 1.8\times10^{-7}\epsilon_p^{-3/2}\langle Z\rangle^2 n_i \log\Lambda_{p|\mathrm{Al}}\,, \tag{2}$$

$$\nu_\perp^{p|e} \approx 1.8\times10^{-7}\epsilon_p^{-3/2} n_e \log\Lambda_{p|e}\,, \tag{3}$$

where ϵ_p is the proton energy (in eV), n_i the aluminium ion number density, n_e the electron number density, $\langle Z\rangle$ the mean aluminium charge, $\log\Lambda_{p|\mathrm{Al}}$ the proton-ion Coulomb logarithm, and $\log\Lambda_{p|e}$ the proton-electron Coulomb logarithm. If Coulomb collisions are sufficiently weak for the protons' velocities to be only slightly perturbed before they traverse the whole plasma (assumed path length $\ell_{n\perp}$), it follows from (1) that

$$\Delta v_\perp \approx V_0\sqrt{\left(\nu_\perp^{p|\mathrm{Al}}+\nu_\perp^{p|e}\right)t_{\mathrm{cross}}} \approx \sqrt{\left(\nu_\perp^{p|\mathrm{Al}}+\nu_\perp^{p|e}\right)\ell_{n\perp}V_0}\,, \tag{4}$$

where $t_{\mathrm{cross}} \approx \ell_{n\perp}/V_0$ is the time taken by the proton beam to traverse the plasma. The characteristic scattering angle $\Delta\theta_{\mathrm{coll}}$ associated with collisional interactions is then given by

$$\Delta\theta_{\mathrm{coll}} \approx \frac{\Delta v_\perp}{V_0} \approx \sqrt{\frac{\left(\nu_\perp^{p|\mathrm{Al}}+\nu_\perp^{p|e}\right)\ell_{n\perp}}{V_0}}\,. \tag{5}$$

For any proton scattering process with characteristic scattering angle $\Delta\theta \ll 1$, it can be shown using kinetic theory [5] that the proton-flux distribution measured on the detector in a proton-imaging diagnostic set-up is the convolution of the proton-flux distribution in the absence of that scattering process with a Gaussian point-spread function, whose full-half-width maximum (FHWM) $a_{\rm res}$ is given by $a_{\rm res} \approx 2.2 r_s \Delta\theta$, where r_s is the distance from the plasma to the detector. Assuming the scattering process is collisional scattering, (5) gives

$$a_{\rm res} \approx 2.2 r_s \sqrt{\frac{\left(\nu_\perp^{p|{\rm Al}} + \nu_\perp^{p|e}\right)\ell_{n\perp}}{V_0}}\,. \tag{6}$$

Now substituting (3), we obtain

$$a_{\rm res} \approx 0.045 \left[\frac{r_s}{10\,{\rm cm}}\right]\left[\frac{\epsilon_p}{4.7\,{\rm MeV}}\right]^{-1}\left[\frac{\ell_{n\perp}}{0.25\,{\rm cm}}\right]^{1/2}\left[\frac{n_e}{4\times10^{19}\,{\rm cm}^{-3}}\right]^{1/2}\left[\frac{\langle Z\rangle}{11}\frac{\log\Lambda_{p|{\rm Al}}}{6} + \frac{\log\Lambda_{p|e}}{6}\right]^{1/2}\,{\rm cm}, \tag{7}$$

where $\langle Z\rangle$ and the Coulomb logarithms are calculated using the characteristic parameters of the beam and plasma. Taking account of the proton-imaging magnification factor $\mathcal{M} = 13/3$, this means that wavenumber cutoff $k_{\rm res}$ due to collisional broadening is given by

$$k_{\rm res} \approx 4.4\mathcal{M}/a_{\rm res} \approx 400\,{\rm cm}^{-1}\,. \tag{8}$$

Measuring the interaction-region plasma's electron number density

With the relationship between the proton-image resolution and electron number-density determined in the previous section, we explain how we construct a predictive model of the high-wavenumber tail of the spectrum of the sharp, large-amplitude proton-flux inhomogeneities (known as caustics) that arise in the 4.7 MeV proton images of the interaction-region plasma at a given electron number density – and thereby measure the interaction-region plasma's number density. We first calculate the one-dimensional spectrum $E_{\delta\Psi}(k)$ of the relative flux distribution – that is, the spectrum of $\delta\Psi \equiv (\Psi - \Psi_0)/\Psi_0$, where Ψ is the actual proton-flux distribution, and Ψ_0 is the mean proton flux – for particular regions of the 4.7 MeV proton images attained in the experiment once the interaction-region plasma has formed. We then assume that the measured spectrum can be expressed in the following manner:

$$E_{\delta\Psi}^{4.7\,{\rm MeV}}(k) = E_{\delta\hat{\Psi}}^{4.7\,{\rm MeV}}(k)\exp\left[-\frac{k^2}{k_{\rm res}^2(\epsilon_p = 4.7\,{\rm MeV})}\right] + E_{\rm noise}(\epsilon_p = 4.7\,{\rm MeV})\,, \tag{9}$$

where $E_{\delta\Psi}^{4.7\,{\rm MeV}}(k)$ is the measured spectrum from the 4.7 MeV proton image, $E_{\delta\hat{\Psi}}^{4.7\,{\rm MeV}}(k)$ is the 'true' spectrum of the large-amplitude flux inhomogeneities in the absence of both collisions and image noise in the 4.7 MeV proton image, $k_{\rm res}(\epsilon_p = 4.7\,{\rm MeV})$ is the collisional wavenumber cutoff for 4.7 MeV protons, and $E_{\rm noise}(\epsilon_p = 4.7\,{\rm MeV})$ is the noise level for the 4.7 MeV proton image. Next, we use the fact that the high-wavenumber tail of the true spectrum of caustics (with characteristic separation scale $\ell_\Psi \gg k^{-1}$) is given by $E_{\delta\hat{\Psi}}^{4.7\,{\rm MeV}}(k) \approx E_{\delta\hat{\Psi},0}(k\ell_\Psi)^{-1}$, where $E_{\delta\hat{\Psi},0}$ is a normalisation constant chosen so that the the low-wavenumber part of the measured and true spectra coincide [5]. We can then use (9) to give an expression for $E_{\delta\Psi}^{4.7\,{\rm MeV}}(k)$ in terms of the two constants $E_{\delta\hat{\Psi},0}$ and $E_{\rm noise}(\epsilon_p = 4.7\,{\rm MeV})$, which can be determined directly from the data, and $k_{\rm res}(\epsilon_p = 4.7\,{\rm MeV})$, which is a function of n_e:

$$E_{\delta\Psi}^{4.7\,{\rm MeV}}(k) \approx \frac{E_{\delta\hat{\Psi},0}}{k\ell_\Psi}\exp\left[-\frac{k^2}{k_{\rm res}^2(\epsilon_p = 4.7\,{\rm MeV})}\right] + E_{\rm noise}(\epsilon_p = 4.7\,{\rm MeV})\,. \tag{10}$$

This is the model used in Figure 8 to predict the 4.7 MeV relative-flux spectrum for a particular electron number density.

Having established a model for the spectrum of caustic structures that we observe in our proton images, we now measure the electron density of the interaction-region plasma as follows. First, for two regions in a given image 4.7 MeV proton image of the interaction-region plasma (see Figure 8, left column), we measure $E_{\delta\Psi}^{4.7\,{\rm MeV}}(k)$. Then assuming that the interaction-region plasma is approximately homogeneous (an assumption validated using X-ray imaging diagnostics used for related experiments on other laser facilities [6, 7]), we use the model (10) and the measured values of $E_{\delta\hat{\Psi},0}$ and $E_{\rm noise}(\epsilon_p = 4.7\,{\rm MeV})$ to construct a prediction for $E_{\delta\Psi}^{4.7\,{\rm MeV}}(k)$ in each region at a

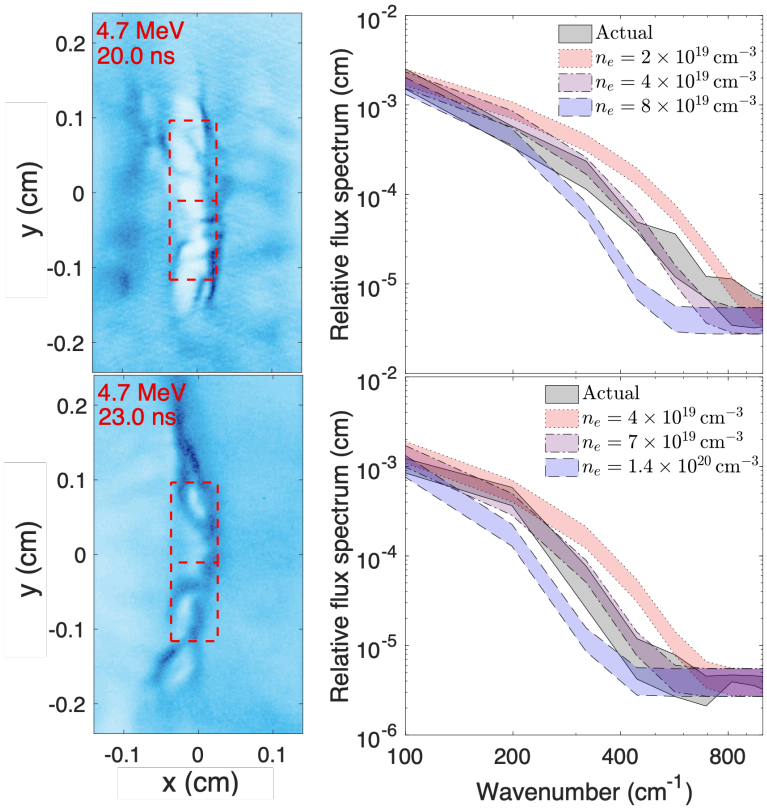

Supplementary Figure 8: *Measurement of the electron number-density of the interaction-region plasma.* Left: samples from 4.7 MeV proton image at $t = 20.0$ ns (top) and $t = 23.0$ ns (bottom), with the same normalizations as for Figure 1 of the main text. Right: spectrum of relative 4.7 MeV proton flux (black), as well as the predicted spectra determined by our model at three different electron number densities, at $t = 20.0$ ns (top) and $t = 23.0$ ns (bottom). The mean and the error for each spectrum are calculated by combining the individual results from the regions demarcated by the dashed red lines.

particular value of n_e. We then assume that the two regions can be treated as independent samples of the interaction-region plasma to construct both a mean value of the measured $E_{\delta\Psi}^{4.7\,\mathrm{MeV}}(k)$, and the uncertainty on that value; we do the same for the predicted $E_{\delta\Psi}^{4.7\,\mathrm{MeV}}(k)$ at different electron number densities (see Figure 8, right column). Finally, we determine the value of n_e at which the measured and predicted spectra agree best, and also the range of values of n_e for which the measured and predicted spectra agree within error; we report the best-fit values in the main text, with the reported uncertainty being derived from the range.

Bounding the electron number density of the counter-propagating plasma jets

In addition to our measurements of the electron number density n_e of the interaction-region plasma, we can also place an upper bound on n_e in each plasma jet prior to collision, based on the absence of collisional scattering of the proton imaging beam. The effective resolution of the 4.7 MeV pre-collision proton images (Figure 9, middle) was the same as for the 8.5 MeV images (Figure 9, left). The characteristic magnitude of the small-scale flux inhomogeneities evident in both images – likely associated with electromagnetic collisionless microinstabilities arising at early times in the experiment [11], before plasma densities rise sufficiently for collisional damping to suppress them – is small, and thus, in the absence of collisions of the proton beam, the Fourier spectrum $E_{\delta\hat{\Psi}}(k)$ of the flux inhomogeneities in both images is the same, up to a scaling factor equal to the ratio of the beam-proton energies (viz., $E_{\delta\hat{\Psi}}(k) \propto \epsilon_p^{-1}$) [5]. This is indeed the case for our data (see Figure 9, right). Writing down an expression analogous to (9) for the 8.5 MeV protons,

$$E_{\delta\Psi}^{8.5\,\mathrm{MeV}}(k) = E_{\delta\hat{\Psi}}^{8.5\,\mathrm{MeV}}(k) \exp\left[-\frac{k^2}{k_{\mathrm{res}}^2(\epsilon_p = 8.5\,\mathrm{MeV})}\right] + E_{\mathrm{noise}}(\epsilon_p = 8.5\,\mathrm{MeV})\,, \tag{11}$$

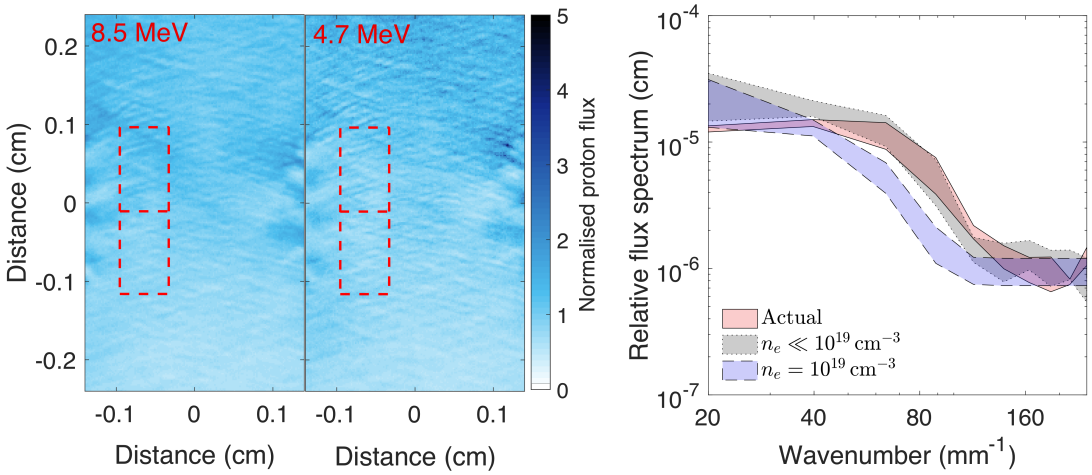

Supplementary Figure 9: *Upper bound on the electron number-density.* Left: samples from 8.5 MeV (far left) and 4.7 MeV (middle left) proton images. Right: spectrum of relative 4.7 MeV proton flux (red), as well as the predicted spectra determined using the 8.5 MeV relative-proton-flux spectrum combined with collisional broadening assuming $n_e = 10^{19}\,\mathrm{cm}^{-3}$ (blue), and with negligible broadening (black). The mean and error for each spectrum are calculated by combining the individual results from the regions demarcated by the dashed red lines.

we can then construct a model for the measured spectrum of small-scale flux inhomogeneities in the 4.7 MeV proton images, given a particular electron number density and the equivalent spectrum in the 8.5 MeV proton images:

$$E_{\delta\Psi}^{4.7\,\mathrm{MeV}}(k) \approx 1.8\left[E_{\delta\Psi}^{8.5\,\mathrm{MeV}}(k) - E_{\mathrm{noise}}(\epsilon_p = 8.5\,\mathrm{MeV})\right] \times \exp\left[\frac{k^2}{k_{\mathrm{res}}^2(\epsilon_p = 8.5\,\mathrm{MeV})} - \frac{k^2}{k_{\mathrm{res}}^2(\epsilon_p = 4.7\,\mathrm{MeV})}\right] + E_{\mathrm{noise}}(\epsilon_p = 4.7\,\mathrm{MeV})\,. \tag{12}$$

For electron number densities $n_e \geq 10^{19}\,\mathrm{cm}^{-3}$, Figure 9, right, shows that the high-wavenumber tail of the 4.7 MeV proton-flux spectrum would be suppressed; we therefore conclude from the absence of any suppression that $n_e \ll 10^{19}\,\mathrm{cm}^{-3}$. This is consistent with the estimates of the electron number density obtained in the FLASH simulation, in which $n_e \approx 10^{18}\,\mathrm{cm}^{-3}$ at the front of each jet [12].

PLASMA CHARACTERIZATION

Calculation of interaction-region plasma parameters

Table II presents a summary (both formulae and values) of key plasma parameters for our experiment, including all those referenced in the main text. The formulae used are derived from [10, 13, 14]; the opacities are calculated using data tables given by [15].

For our reported parameters, the plasma may appear to be well described as being optically thin (λ_P is much larger than the largest spatial dimension of the interaction-region plasma, $\ell_{n\perp} \approx 0.25\,\mathrm{cm}$), and the radiative cooling time is much longer than the turnover time of the plasma turbulence. However, we caution that the Planck opacity for aluminium increases by around three orders of magnitude over the temperature interval $T = 20$ eV to $T = 100$ eV. As a consequence of this, the radiative cooling time for a plasma with the same mass density as given in Table II, but with $T = 50$ eV, is considerably smaller than that at $T = 100$ eV: $\tau_{\mathrm{rad}}(T = 50\,\mathrm{eV}) \approx 1.7\,\mathrm{ns}$ (see Supplementary Figure 10, left). As well as this, for $T \gtrsim 100\,\mathrm{eV}$, the Planck opacity increases as the temperature does (until $T \approx 175\,\mathrm{eV}$); the cooling function increases by nearly two orders of magnitude, giving $\tau_{\mathrm{rad}}(T = 175\,\mathrm{eV}) \approx 1.4\,\mathrm{ns}$. Because the plasma turbulence is both supersonic and has a large Peclet number, it is to be expected that there be both significant density and temperature variations in the interaction-region plasma; as a consequence, we cannot rule out the possibility that radiative cooling plays a significant role in the turbulent plasma's dynamics. We do, however, observe that the characterisation of the plasma as being optically thin remains appropriate, even in the

Quantity	Formula	Value
Aluminium mass (M)		27
Mean aluminium charge ($\langle Z \rangle$)		$\sim$11
Temperature (T)		100 eV
Electron number density (n_e)		7×10^{19} cm^{-3}
Aluminium number density (n_i)		6×10^{18} cm^{-3}
Turbulent velocity ($u_{\rm turb}$)		$2{\times}10^{7}$ cm s^{-1}
Outer scale (L)		0.04 cm
Magnetic field (B)		10 kG
Adiabatic index (γ_I)		5/3
Coulomb logarithm ($\log \Lambda$)	$23.5 - \log n_e^{1/2} T^{-5/4} - \sqrt{10^{-5} + (\log T - 2)^2/16}$	~ 6
Mass density (ρ)	$1.7 \times 10^{-24} M n_e / \langle Z \rangle$	2.9×10^{-4} g cm^{-3}
Debye Length ($\lambda_{\rm D}$)	$7.4 \times 10^2\, T^{1/2}\, (1 + \langle Z \rangle)^{-1/2}\, n_e^{-1/2}$	2.5×10^{-7} cm
Sound speed ($c_{\rm s}$)	$9.8 \times 10^5\, [(\langle Z \rangle + 1) \gamma_I T]^{1/2} M^{-1/2}$	8×10^6 cm s^{-1}
Mach number	$u_{\rm turb}/c_{\rm s}$	2.5
Plasma β	$4.0 \times 10^{-11} \left(1 + \langle Z \rangle^{-1}\right) n_e T / B^2$	3×10^3
Ion-ion mean free path (λ_{ii})	$2.9 \times 10^{13}\, T^2 / \langle Z \rangle^3 n_e \log \Lambda$	5×10^{-7} cm
Electron-ion mean free path (λ_e)	$2.1 \times 10^{13}\, T^2 / \langle Z \rangle n_e \log \Lambda$	5×10^{-5} cm
Electron-ion equilibration time (τ_{ie}^{ϵ})	$3.1 \times 10^8\, M T^{3/2} / \langle Z \rangle n_e \log \Lambda$	4×10^{-9} s
Electron Larmor radius (ρ_e)	$2.4\, T^{1/2}/B$	2.4×10^{-3} cm
Ion Larmor radius (ρ_i)	$1.0 \times 10^2\, M^{1/2} T^{1/2} / \langle Z \rangle B$	5×10^{-2} cm
Thermal diffusivity (χ)	$4 \times 10^{21}\, T^{5/2} / \langle Z \rangle n_e \log \Lambda$	9.0×10^4 cm^2 s^{-1}
Turbulent Peclet number (Pe)	$u_{\rm turb} L / \chi$	9
Kinematic viscosity (ν)	$1.9 \times 10^{19}\, T^{5/2} / M^{1/2} \langle Z \rangle^3 n_e \log \Lambda$	0.7 cm^2 s^{-1}
Turbulent Reynolds number (Re)	$u_{\rm turb} L / \nu$	10^6
Resistivity (η)	$2.8 \times 10^5\, \langle Z \rangle \log \Lambda / T^{3/2}$	1.8×10^4 cm^2 s^{-1}
Magnetic Reynolds number (Rm)	$u_{\rm turb} L / \eta$	45
Magnetic Prandtl number (Pm)	Rm/Re	4×10^{-5}
Planck Opacity (κ_P)		30 cm^2 g^{-1}
Photon mean free path (λ_P)	$1/\rho\kappa_P$	120 cm
Cooling function (L_Λ)	$1.03 \times 10^{12}\, \rho \kappa_P T^4$	9×10^{17} erg cm^{-3} s^{-1}
Radiative cooling time ($\tau_{\rm rad}$)	$1.4 \times 10^{12} \rho (\langle Z \rangle + 1) T / M L_\Lambda$	2×10^{-8} s

Supplementary Table II: Characteristic parameters in the region of supersonic plasma turbulence. The units system used for all physical quantities in the above formulas is Gaussian CGS, except for the temperature, which expressed in eV.

presence of significant temperature variations. At $T = 50$ eV, the photon mean free path λ_P is given by $\lambda_P \approx 0.5\,$cm (see Figure 10, right), which remains much larger than the scale of temperature variations ($L \approx 400\,\mu$m).

Plasma parameters of supersonic plasma jets prior to collision

In the main text, we report a measurement of the jet velocity $u_{\rm jet} \approx 290\,$km/s that is derived from our time-resolved proton-imaging diagnostic; this value is, in fact, consistent with a estimate derived from heuristic expectations. More specifically, the collision between the counter-propagating jets in our experiment occurs at $t_{\rm coll}$ = 16–19 ns; the temporal delay $\Delta t_{\rm coll}$ between the LMJ drive-beam pulse's midpoint and the jet collision time is therefore $\Delta t_{\rm coll}$ = 13.5–16.5 ns. Using the known distance $\ell_{\rm foil} \approx 0.4$ cm between the aluminium foil and target's center, we can therefore estimate the jet velocity $u_{\rm jet}$ as being $u_{\rm jet} \approx \ell_{\rm foil}/\Delta t_{\rm coll}$; this gives $u_{\rm jet}$ = 240–300 km/s. Reassuringly, our proton-imaging derived measurement of the jet velocity falls inside this range.

We do not have a measurement of the temperature $T_{\rm jet}$ of either jet prior to collision. However, we can estimate $T_{\rm jet}$ in the following manner, using a combination of physical arguments and bespoke FLASH simulations of the LMJ experiment. The latter, which assumed a more efficient laser-foil coupling efficiency than was likely realised in practice, and thus obtained greater jet velocities by a factor of $\sim$2, suggest that the initial jet Mach number $\mathrm{Ma}_{\rm jet}$ of the jet in the experiment satisfies the following bound: $\mathrm{Ma}_{\rm jet} \lesssim 10$. This being the case, we use the known jet

velocity ($u_{\rm jet} \approx 290\,{\rm km/s}$) to estimate

$$T_{\rm jet} \gtrsim 20 \left[\frac{\gamma_I}{5/3}\right]^{-1} \left[\frac{\langle Z_{\rm jet}\rangle + 1}{6}\right]^{-1} \left[\frac{M}{27}\right]^{1/2} \left[\frac{u_{\rm jet}({\rm km/s})}{290\,{\rm km/s}}\right]^{2} {\rm eV}\,, \tag{13}$$

where we have used a Saha ionization model to estimate $\langle Z_{\rm jet}\rangle$ at $T = 20$ eV. If we combine this bound with the physical requirement that $T_{\rm jet} \ll T = 100$ eV (in other words, assume that the plasma jets experience significant heating when they collide), we conclude that $20\,{\rm eV} \lesssim T_{\rm jet} \lesssim 50\,{\rm eV}$. Once these bounds are established, we observe that for the characteristic jet densities ($\rho_{\rm jet} \sim 10^{-5} - 10^{-4}\,{\rm g/cm^3}$), the radiative cooling time $\tau_{\rm rad,jet}$ is approximately $\tau_{\rm rad,jet} \sim 3-10$ ns. This is comparable to the time taken for the jet to travel the distance $\ell_{\rm grid} \approx 0.2\,{\rm cm}$ from the grids in the centre of the target ($t_{\rm grid} \approx \ell_{\rm grid}/u_{\rm jet} \approx 7\,{\rm ns}$). Thus, we conclude that each jet experiences significant cooling as it travels towards its counterpart, and so a reasonable estimate for $T_{\rm jet}$ is the lower bound (13): $T_{\rm jet} \sim 20\,{\rm eV}$.

Using the formula for η given in Table II, we can now estimate the magnetic Reynolds number of either jet: ${\rm Rm_{jet}} \approx u_{\rm jet} L/\eta_{\rm jet} \approx 20$. This justifies the assumption made in the main text that the magnetic field is effectively frozen into the flow of each jet over the timescale $\Delta t_p \approx 300\,{\rm ps}$ separating the two proton species used for imaging the jets.

The role of the Biermann battery in our experiment

The Biermann battery is known to generate significant magnetic fields in colliding laser-plasma jet experiments; here, we elaborate on their importance in our experiment. In the main text, we claim that the subsequent amplification of a stochastic component of the magnetic field observed in our experiment can be attributed to the action of supersonic motions, rather than to the action of the Biermann battery alone. To justify this claim, we consider the induction equation governing the evolution of the magnetic field,

$$\frac{\partial \boldsymbol{B}}{\partial t} = \nabla \times (\boldsymbol{u} \times \boldsymbol{B}) - \frac{ck_B}{en_e} \nabla n_e \times \nabla T_e + \eta \nabla^2 \boldsymbol{B}\,, \tag{14}$$

where k_B is Boltzmann's constant, e is the elementary charge, and c is the speed of light, and compare the respective sizes of the inductive term and the Biermann term just after collision:

$$\frac{|\boldsymbol{u} \times \boldsymbol{B}|}{|ck_B \nabla n_e \times \nabla T_e/en_e|} \sim \left[\frac{\delta n_e}{n_e}\right]^{-1} \left[\frac{B_0({\rm kG})}{10\,{\rm kG}}\right] \left[\frac{T_e({\rm eV})}{100\,{\rm eV}}\right]^{-1} \left[\frac{L({\rm cm})}{0.04\,{\rm cm}}\right] \left[\frac{u_{\rm turb}({\rm cm\ s^{-1}})}{1.9\times 10^7\,{\rm cm\ s^{-1}}}\right]\,. \tag{15}$$

We conclude that the terms are comparable, provided that both the variations in density and in temperature are comparable to their mean values.

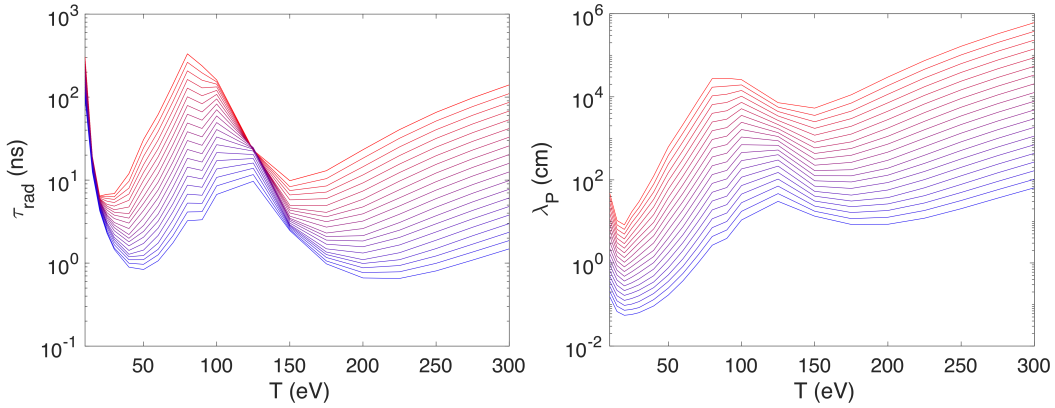

Supplementary Figure 10: *Radiative properties of aluminium plasma relevant to our experiment.* Left: radiative cooling time (calculated using the formula given in Supplementary Table II), plotted as a function of temperature. The 20 different lines plotted correspond to this curve at different mass densities, with $\rho_{\rm min} = 10^{-5}\,{\rm g\,cm^{-5}}$, and $\rho_{\rm max} = 10^{-3}\,{\rm g\,cm^{-3}}$, and equal logarithmic spacing. Right: same as left, but showing photon mean free path.

RELATIONSHIP OF RESULTS TO PREVIOUS EXPERIMENTS

In the main text, we reference several previous laser-plasma experiments that reported turbulent amplification of magnetic fields [6, 7, 16, 18], and one which reported creating boundary-free supersonic turbulence without observing amplification [17]; here, we outline in more detail the relationship between these experiments and the experiment reported in this paper. Table III provides a summary of the key physical parameters which were attained in the experiments at times coincident with the observation of magnetic-field amplification. The parameters reported here

Experiment	Identifier	L(cm)	Rm	Pm	$\mathrm{Ma}_{\mathrm{turb}}$	$\delta B/B_0$	$E_{\mathrm{mag}}/E_{\mathrm{kin}}$
This paper	LMJ	0.04	45	$\sim 4\times10^{-5}$	2.5	∼1-2	10^{-4}
Meinecke et al. [16]	Vulcan A	0.2-0.5	3-7	$\sim 10^{-5}$	$\lesssim 1$	∼1-3	2×10^{-7}
White et al. [17]	Vulcan B	0.2	$\lesssim 1$	$\sim 10^{-5}$	1–6	< 1	2×10^{-3}
Tzeferacos et al. [6]	OMEGA A	0.06	$\lesssim 600$	0.2-0.5	0.5	∼30	0.04
Bott et al. [7]	OMEGA B	0.04	$\lesssim 450$	1-3	0.5	∼20	0.03
Meinecke et al. [18]	NIF	0.06	2000–6000	3–50	0.6	~ 13	0.09

Supplementary Table III: Plasma parameters attained in experiments that have investigated turbulent amplification of magnetic fields in laser plasmas. Here, L is the driving scale of turbulent motions in the plasma; we note that in [16], the reported magnetic Reynolds number is instead defined with the scale length of the entire turbulent plasma.

have all been calculated using consistent definitions of relevant quantities (e.g., the length scales used in the fluid and magnetic Reynolds numbers); we caution readers that the conventions (and notation) employed in the original papers are not all consistent with each other. For convenience, we refer to each experiment via an identifier: the name of the laser facility at which the experiment was carried out.

While amplification of magnetic fields is seen in all of the experiments, it is much more significant in the NIF, OMEGA A and OMEGA B experiments than in our LMJ experiment, or in the Vulcan experiment. The obvious difference between these two sets of experiments is the values of Rm and Pm. More specifically, for the LMJ and Vulcan experiments, Rm is likely to be below the critical value Rm_c required for the turbulent dynamo to operate in the $\mathrm{Pm} \ll 1$ regime. In the OMEGA and NIF experiments, that critical threshold seems to have been successfully surpassed (indeed, in OMEGA B and NIF we anticipate that the greater than order-unity value of Pm reduces Rm_c significantly).

The similar degree of amplification seen in the LMJ experiment and in the Vulcan A experiment, in spite of the significantly smaller values of Rm obtained in the latter, suggests that another factor must be affecting the efficacy of the amplification mechanism in our experiment. As discussed in the main text, a plausible candidate is the turbulent Mach number. The Vulcan B experiment suggests that the turbulent Mach number of the plasma increases significantly with time [17]; when comparing to our experiment, it is therefore necessary to determine the turbulent Mach number attained in the Vulcan experiment at comparable times to the peak field amplification (at $t = 950$ ns). Since this number is not reported in [16], we make this determination using validated FLASH MHD simulations of the Vulcan experiment. Figure 11 shows slice plots of the density and magnetic field at $t = 950$ ns, as well as the sound speed and (one component of) the velocity in the interaction-region plasma. Taking a lineout across the interaction-region plasma, and comparing the mean turbulent velocity and mean sound speed, we find that, on average, $\mathrm{Ma}_{\mathrm{turb}} = u_{\mathrm{turb}}/c_s \approx 1$. We conclude that amplification in the Vulcan A experiment does not occur in the supersonic regime, whereas it does in the LMJ experiment. This difference likely explains why the LMJ experiment saw similar field amplification to the Vulcan A experiment, in spite of much greater characteristic values of Rm in the former.

[1] C. Fauquignon, and F. Floux, Phys. Fluids **13**, 386 (1970).

[2] D.E. Fratanduono, T.R. Boehly, P.M. Celliers, M.A. Barrios, J.H. Eggert, R.F. Smith, D.G. Hicks, G.W. Collins, and D.D. Meyerhofer, J. Appl. Phys. **110**, 073110 (2011).

[3] C.E. Max, *Physics of Laser Fusion. Vol. I. Theory of the Coronal Plasma in Laser-Fusion Targets Rep. No. UCRL-53107*, Lawrence Livermore National Laboratory, 1981.

[4] S. Agnostinelli *et. al.*, Nucl. Instrum. Meth. A **506** 250 (2003).

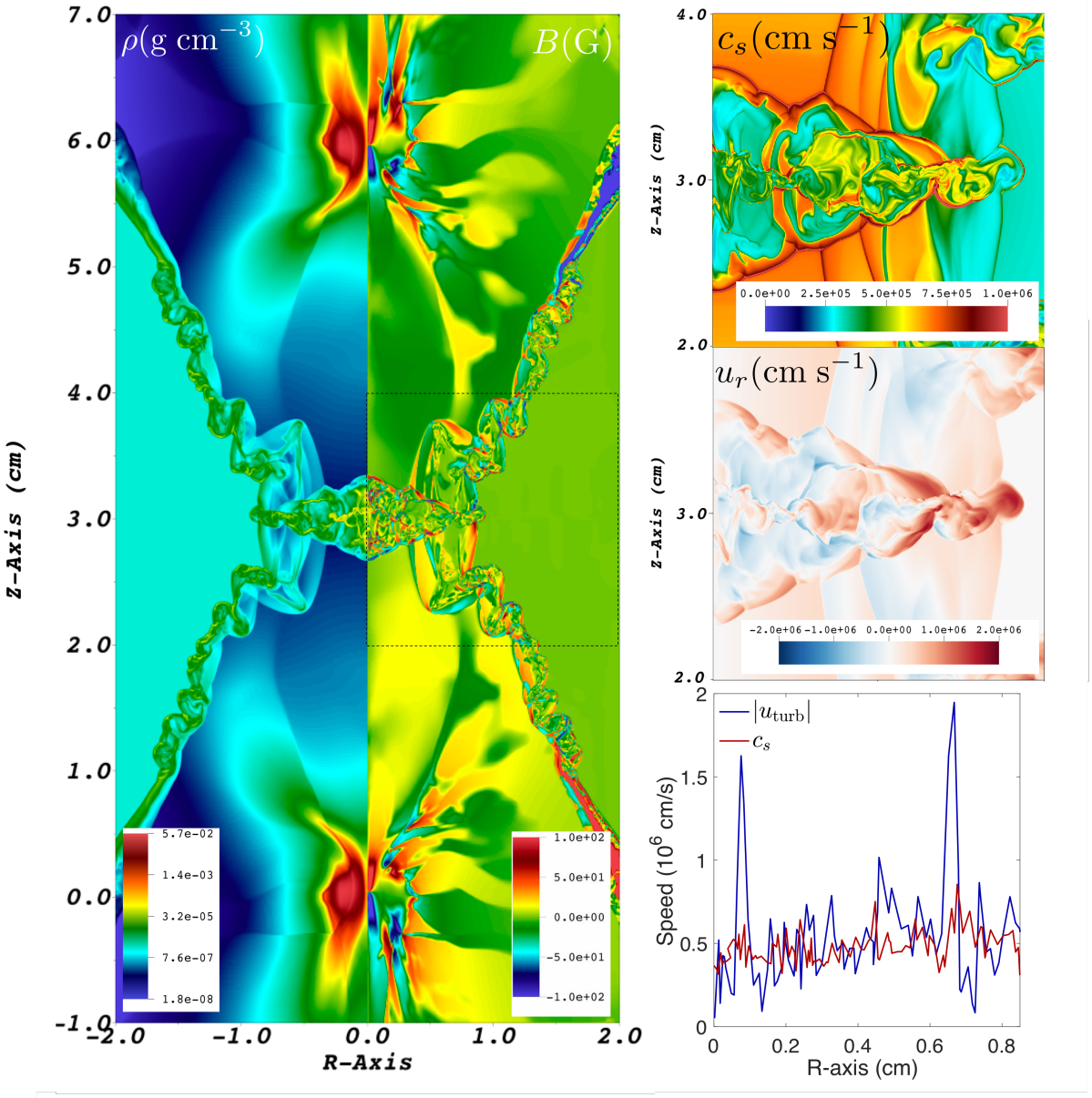

Supplementary Figure 11: *Establishing turbulent Mach number of Vulcan experiment using FLASH simulations.* The simulations are two dimensional, and cylindrically symmetric (full details are provided in [16]). Left panel: slice plots of density and magnetic field strength at time ($t = 950$ ns) at which peak field strengths are attained. Top right panel: sound speed c_s calculated using the formula given in Table II at the same time; the plasma is a carbon-argon mixture whose composition varies with position, so the simulated values of M and $\langle Z \rangle$ are determined from the simulation. Middle right panel: radial component of velocity. Bottom right panel: lineout (taken at $Z = 3.0$ cm) of the sound speed and the total turbulent velocity (including both radial and axial components).

[5] A.F.A. Bott, C. Graziani, T.G. White, P. Tzeferacos, D.Q. Lamb, G. Gregori, and A.A. Schekochihin, J. Plasma Phys. **83** 6 (2017).
[6] P. Tzeferacos *et al.*, Nat. Comm. **9**, 591 (2018).
[7] A.F.A. Bott *et al.*, Proc. Nat. Acad Sci. USA, **118**, e2015729118 (2021).
[8] L. Chen *et al.*, Astrophys. J. **892**, 114 (2020).
[9] F. Nürnberg, M. Schollmeier, E. Brambrink, A. Blažević, D.C. Carroll, K. Flippo, D.C. Gautier, M. Geissel, K. Harres, B.M. Hegelich, O. Lundh, K. Markey, P. McKenna, D. Neely, J. Schreiber, and M. Roth, Rev. Sci. Instrum. **80**, 033301

(2009).
[10] J.D. Huba, *NRL Plasma Formulary* (Naval Research Laboratory, Washington DC, 1994).
[11] CM Huntington *et. al.*, Nat. Phys **11**, 173 (2015)
[12] B. Khiar, P. Tzeferacos, A.F.A. Bott, A.A. Schekochihin, A. Casner, G. Gregori, and D.Q. Lamb, In prep. (2020).
[13] S. Braginskii, Rev. Plasma Phys. **1**, 205 (1965).
[14] J.E. Cross, B. Reville, G. Gregori. Astrophys. J. **795**, 59 (2014).
[15] J. Abdallah Jr., and R.E.H. Clark, *TOPS: A Multigroup Opacity Code; Los Alamos Report LA-10454.*
[16] J. Meinecke *et al.*, Proc. Nat. Acad. Sci. USA **112**, 8211 (2015).
[17] T.G. White *et. al.*, Nature Comm. **10**, 1758 (2019).
[18] J. Meinecke *et al.*, arXiv:2105.08461 (2021).